

---

# Multi-Level Monte Carlo Training of Neural Operators

---

**James Rowbottom\***

Department of Applied Mathematics  
and Theoretical Physics  
University of Cambridge  
Cambridge, CB3 0WA UK  
jr908@cam.ac.uk

**Stefania Fresca\***

MOX Lab - Department of Mathematics  
Politecnico di Milano  
Milano, I-20133  
stefania.fresca@polimi.it

**Pietro Lio**

Department of Computer Science  
and Technology  
University of Cambridge  
Cambridge, CB3 0FD UK  
pl219@cam.ac.uk

**Carola-Bibiane Schönlieb**

Department of Applied Mathematics  
and Theoretical Physics  
University of Cambridge  
Cambridge, CB3 0WA UK  
cbs31@cam.ac.uk

**Nicolas Boullé**

Department of Mathematics  
Imperial College London  
London, SW7 2AZ UK  
n.boullé@imperial.ac.uk

## Abstract

Operator learning is a rapidly growing field that aims to approximate nonlinear operators related to partial differential equations (PDEs) using neural operators. These rely on discretization of input and output functions and are, usually, expensive to train for large-scale problems at high-resolution. Motivated by this, we present a Multi-Level Monte Carlo (MLMC) approach to train neural operators by leveraging a hierarchy of resolutions of function discretization. Our framework relies on using gradient corrections from fewer samples of fine-resolution data to decrease the computational cost of training while maintaining a high level accuracy. The proposed MLMC training procedure can be applied to any architecture accepting multi-resolution data. Our numerical experiments on a range of state-of-the-art models and test-cases demonstrate improved computational efficiency compared to traditional single-resolution training approaches, and highlight the existence of a Pareto curve between accuracy and computational time, related to the number of samples per resolution.

## 1 Introduction

Neural operators have been recently introduced as a mathematical tool to learn infinite-dimensional operators, mapping functions to functions, and have been applied in many scientific areas to approximate the solution operator of partial differential equations (PDEs) or solve inverse problems [Li et al., 2021b, Lu et al., 2021, Kovachki et al., 2023, Boullé and Townsend, 2024, Kovachki et al.,

---

\*Equal contribution

2024]. Several neural operator architectures have been proposed including Fourier neural operators (FNOs) [Li et al., 2021b], deep operator networks (DeepONets) [Lu et al., 2021], graph neural operators [Pfaff et al., 2020, Anandkumar et al., 2020] and transformers [Cao, 2021, Hao et al., 2023]. These networks exploit (or enforce) different properties of operators such as regularity of solutions and geometry of the underlying spatial domain on which functions are defined, and are supported by various approximation theory results [Kovachki et al., 2021, 2024, Lanthaler et al., 2022].

The simulation of physical systems often relies on mesh-based representations, where the choice of mesh resolution presents a fundamental trade-off between computational cost and accuracy (this appears explicitly in, e.g., finite element error estimations [Brenner and Scott, 2008]). Approximated solutions discretized on fine meshes are more accurate, but they significantly increase computational overhead during both training and inference. Although traditional deep learning approaches typically operate at a fixed resolution, limiting their ability to efficiently learn across multiple scales, neural operators are generally designed to process functions defined on arbitrary meshes by learning a representation with respect to a given basis [Li et al., 2021b, Bouziani and Boullé, 2024] and interpolating/projecting across different resolutions. One of the main challenges in scaling neural operators to large-scale three-dimensional problems is the computational cost of the training phase, due to the fine gradient estimations needed to update the parameters of the neural network with a gradient-based optimization algorithm. Little work has been done in the literature on efficient training of neural operators, with the exception of a few works that proposed multi-scale architectures [Li et al., 2020, He et al., 2024, Bouziani and Boullé, 2024].

This work addresses the problem of the high training cost of neural operators on high-resolution data by proposing a flexible gradient estimation algorithm based on Multi-Level Monte Carlo (MLMC) methods [Giles, 2008, Giles and Waterhouse, 2009, Cliffe et al., 2011, Giles, 2015] cast in the framework of mini-batch stochastic optimization. Our framework allows us to estimate the expectation of the gradients of the loss function on the finest resolution with respect to the neural network parameters using a multi-resolution approach. This quantity is expressed as a telescopic sum of gradients expectations across mesh levels. The aim is to drastically decrease the training computational time by capturing the most of the dynamics, i.e., the variance, on the coarse grid, hence decreasing the number of gradient computations needed on the finest grid. We proved that the main assumptions of the MLMC theory are satisfied, under suitable regularity properties, by neural operators thus providing a robust mathematical justification in its application to operator learning. Moreover, our algorithm introduces a notion of “pareto optimality” in the training process, where one can adjust the number of resolution levels (and hence the number of samples across levels) to achieve a trade-off between training time computational cost and accuracy.

**Related Works.** Our work translates the classic MLMC methods for PDEs [Giles, 2008, Giles and Waterhouse, 2009, Cliffe et al., 2011, Giles, 2015] to the context of neural operators, where the regularity properties of the PDE solution theoretically justify the approximation of the gradients. MLMC methods also inspired the development of several related works in machine learning. In [Li et al., 2021a] an active learning strategy is employed to dynamically query an acquisition function to process new examples at different resolutions. Lye et al. [2021] propose a multi-level approach to learn input parameters to observable maps and apply it to uncertainty quantification. Moreover, Jin et al. [2023] study a multi-level operator learning algorithm to obtain theoretical sample complexity estimates. More recently, Gal et al. [2025], Zakariaei et al. [2025] introduce a multi-scale stochastic gradient descent approach to train convolutional and graph neural networks at different resolutions.

**Main contributions.** The key advantages and novelties of this work are summarized below:

- Introduction of a rigorous mathematical framework supporting the adoption of MLMC training of neural operators at different resolutions.
- Exploitation of multi-resolution data for the acceleration of training with a single high-resolution dataset, by coarsening, or when access to high-resolution data is limited or scarce.
- Implementation of data batching engine that enables effective training with multi-resolution dataset and allows different sampling strategies.
- Reduction of training time by up to 60% compared to single-resolution training across multiple state-of-the-art neural operators architectures and test problems.

## 2 Multi-Level Monte Carlo method

Our approach extends the MLMC framework to neural networks training. In particular, we aim at accelerating the training of neural operators by using a multi-resolution approach, i.e., the MLMC paradigm. MLMC methods stand on the idea that most of the uncertainty can be captured on the coarse grids and so the number of samples needed on the finest grid is greatly reduced.

### 2.1 Mathematical Framework

We follow the neural operator framework introduced by Kovachki et al. [2023] and consider two Hilbert spaces of functions  $\mathcal{A}$  and  $\mathcal{U}$ , respectively, defined on bounded domains  $\Omega_{\mathcal{A}} \subset \mathbb{R}^d$  and  $\Omega_{\mathcal{U}} \subset \mathbb{R}^d$ . We aim to approximate a (nonlinear) operator  $\mathcal{G}^\dagger : \mathcal{A} \rightarrow \mathcal{U}$  mapping between these spaces using a neural operator  $\mathcal{G}_\theta : \mathcal{A} \rightarrow \mathcal{U}$ , parametrized by a finite number of parameters  $\theta \in \mathbb{R}^p$ . We train the neural operator using pairs of observations  $\{a^{(j)}, u^{(j)}\}_{j=1}^N$ , where  $a^{(j)} \sim \mu$  are sampled i.i.d. from a probability measure  $\mu$  supported on  $\mathcal{A}$  (usually a Gaussian measure), and aim to control the  $L^2_\mu(\mathcal{A}; \mathcal{U})$  Bochner norm as

$$\|\mathcal{G}^\dagger - \mathcal{G}_\theta\|_{L^2_\mu(\mathcal{A}; \mathcal{U})}^2 = \mathbb{E}_{a \sim \mu} \|\mathcal{G}^\dagger(a) - \mathcal{G}_\theta(a)\|_{\mathcal{U}}^2 = \int_{\mathcal{A}} \|\mathcal{G}^\dagger(a) - \mathcal{G}_\theta(a)\|_{\mathcal{U}}^2 d\mu(a).$$

Here, we assume that both  $\mathcal{G}^\dagger$  and  $\mathcal{G}_\theta$  are  $\mu$ -measurable, belong to  $L^2_\mu(\mathcal{A}; \mathcal{U})$ , and wish to solve the following optimization problem:

$$\min_{\theta \in \mathbb{R}^p} \mathbb{E}_{a \sim \mu} \|\mathcal{G}^\dagger(a) - \mathcal{G}_\theta(a)\|_{\mathcal{U}}^2,$$

using a gradient-based algorithm as

$$\theta^{k+1} = \theta^k - \alpha \nabla_\theta (\mathbb{E}_{a \sim \mu} \|\mathcal{G}^\dagger(a) - \mathcal{G}_\theta(a)\|_{\mathcal{U}}^2), \quad (1)$$

where we move the gradient inside the expectation using the dominated convergence theorem (see. Eq. (4) in Appendix A), and denote by  $X_\theta : \mathcal{A} \rightarrow \mathbb{R}$  the operator defined as  $X_\theta(a) = \|\mathcal{G}^\dagger(a) - \mathcal{G}_\theta(a)\|_{\mathcal{U}}^2$ .

**Function space hierarchy.** For  $1 \leq i \leq m$ , we define  $\mathcal{A}_i$  to be a finite element space of functions defined on a mesh  $\Omega_{\mathcal{A}}^i$  of  $\Omega_{\mathcal{A}}$ , with polynomial degree  $k \geq d/2$ , and mesh diameter  $h_i = 2^{-i} h_0 > 0$  such that  $\dim(\mathcal{A}_1) \leq \dots \leq \dim(\mathcal{A}_m)$  (note that one could use another refinement factor). For simplicity, we assume that  $\mathcal{A}_i$  are subspaces of  $\mathcal{A}$  so that the injection operator  $\mathcal{A}_i \rightarrow \mathcal{A}$  is trivial, and define the Galerkin projection operator  $\mathcal{P}_i : \mathcal{A} \rightarrow \mathcal{A}_i$  and  $X_\theta^i = X_\theta \circ \mathcal{P}_i$ . Note that the neural operator  $\mathcal{G}_\theta$  is discretization invariant following the framework introduced in [Kovachki et al., 2023], and that computing  $X_\theta^1 \circ \mathcal{P}_1$  (and its gradient with respect to  $\theta$ ) is inherently cheaper than computing  $X_\theta^m \circ \mathcal{P}_m$ . Hence, the projection step to the latent dimension of the neural operator is computationally cheaper. Note that this applies for any neural operator architecture written in the encoder-processor-decoder framework [Bouziani and Boullé, 2024, Kovachki et al., 2024]. FNOs [Li et al., 2021b] could also be written in this framework by considering a spectral discretization of the function space, and the Fourier transform as the encoder.

**Multi-Level Monte Carlo gradient estimation.** The goal of the MLMC [Giles, 2015] gradient estimation is to approximate the expectation of the gradient of the loss function with respect to the neural network parameters  $\theta$  using a telescopic sum of differences across mesh levels. The main idea is to use a coarse mesh to capture most of the variance in the gradient, and then use finer meshes to correct for the remaining variance. This allows us to reduce the number of fine-mesh samples needed, thus speeding up the training process. We express the fine-mesh gradient expectation as a telescopic sum of differences across mesh levels and decompose the expectation of the gradient in Eq. (4) as follows:

$$\begin{aligned} \mathbb{E}_{a \sim \mu} [\nabla_\theta X_\theta^m(a)] &= \mathbb{E}_{a \sim \mu} [\nabla_\theta X_\theta^1(a)] + \sum_{i=2}^m \mathbb{E}_{a \sim \mu} [\nabla_\theta X_\theta^i(a) - \nabla_\theta X_\theta^{i-1}(a)] \\ &\approx \frac{1}{N_1} \sum_{j=1}^{N_1} [\nabla_\theta X_\theta^1(a_{1,j})] + \sum_{i=2}^m \left( \frac{1}{N_i} \sum_{j=1}^{N_i} [\nabla_\theta X_\theta^i(a_{i,j}) - \nabla_\theta X_\theta^{i-1}(a_{i,j})] \right), \end{aligned} \quad (2)$$

where  $\{N_i\}_{1 \leq i \leq m}$  denotes the sample sizes at each level. Note that we do not consider discretization of the output space  $\mathcal{U}$  for simplicity, but a similar argument would also work, see, e.g., [Bouziani and Boullé, 2024]. The following proposition relies on a standard MLMC result [Giles, 2008, Giles and Waterhouse, 2009] and provides a mean squared error bound for the MLMC estimator in Eq. (2). The proof is deferred to Appendix A.

**Proposition 2.1.** *Assume that  $\mu$  is compactly supported on  $H^k(\Omega_{\mathcal{A}})$ , and that the cost of each sample in Eq. (2) scales linearly with respect to the number of degrees of freedom in the finite element space as  $C_i = \mathcal{O}(k^d 2^{di})$  for  $1 \leq i \leq m$ . For any  $\epsilon > 0$ , under enough regularity on  $\mathcal{G}^1$  and  $\mathcal{G}_\theta$ , there exist a number of levels  $m > 0$  and an optimal allocation of samples  $N_i \propto 2^{-(2k+d)i/2}$  per level such that the MLMC estimator given by Eq. (2) has a mean squared error bounded by  $\epsilon^2$ .*

Following Proposition 2.1, we find that one can reduce the number of fine-mesh samples to accurately estimate the gradient of the loss function by adapting the number of samples at each level depending on the mesh resolution. Note that the number of samples per resolution is related to the sample cost assumption, which depends on the type of neural operator architecture. The analysis can also be generalized to non-geometric hierarchy of meshes [Haji-Ali et al., 2016].

*Remark 2.2. (Multi-Level Quasi-Monte Carlo)* The computational cost of MLMC can be reduced by employing a Quasi-Monte Carlo (QMC) approach, where a nested set of samples across mesh resolutions is chosen instead of independent realizations at each level [Kuo et al., 2012, 2015]. This increases the variance of the estimator but results in a lower cost complexity [Giles, 2015].

## 2.2 Mini-batch strategies

The mathematical framework presented in Section 2.1 is based on the Gradient Descent (GD) algorithm for training neural networks. However, mini-batching is commonly used in practice due to its advantages in computational efficiency, generalization performance, and scalability. In this context, the MLMC gradient estimation (see Eq. (2)), which adjusts the amount of samples across resolution levels, naturally extends to mini-batch training and reads as follows:

$$\mathbb{E}_{a \sim \mu}[\nabla_\theta X_\theta^m(a)] \approx \frac{1}{B_1} \sum_{j=1}^{B_1} [\nabla_\theta X_\theta^1(a_{1,j})] + \sum_{i=2}^m \left( \frac{1}{B_i} \sum_{j=1}^{B_i} [\nabla_\theta X_\theta^i(a_{i,j}) - \nabla_\theta X_\theta^{i-1}(a_{i,j})] \right), \quad (3)$$

where  $B_i$  stands for the batch size at correction level  $i$  in the sum hierarchy, which is obtained by drawing samples from a subset of  $N_i$  observations at resolution  $R_i$ , for  $1 \leq i \leq m$ . The correction term  $-\nabla_\theta X_\theta^{i-1}(a_{i,j})$  in Eq. (3) is computed by coarsening the sample  $a_{i,j}$  to resolution  $R_{i-1}$  and evaluating the neural operator. Following Section 2.1, we decrease  $B_i$  and  $N_i$  with respect to the level  $i$  as the data resolution  $R_i$  increases.

**Sample and batch sizes.** We denote by  $\mathcal{N}_i = \{(a_{i,j}, u_{i,j})\}_j$  the set of data observations at level  $i$ , and by  $N$  the total number of samples. We determine the evolution of the number of samples  $N_i = |\mathcal{N}_i|$  according to one of the following approaches:

- *Geometric progression.* There is a constant growing factor  $\delta \geq 1$  between a level  $i$  and a subsequent level  $i + 1$  as  $N_i = \delta N_{i+1}$ , for  $1 \leq i \leq m - 1$ , such that  $\sum_{i=1}^m N_i \approx N$ .
- *Prescribed progression.* We manually select the amount of samples at level  $i$  as  $N_i$ , such that  $N_m \leq \dots \leq N_1$  and  $\sum_{i=1}^m N_i = N$ .
- *Optimal progression.* The evolution of samples follows the “optimal” geometric progression  $N_i = 2^{-(2k+d)i/2} N_{i+1}$  determined by Proposition 2.1.

Note that while Proposition 2.1 provides an optimal choice for the allocation of samples, the geometric factor intrinsically depends on the sampling cost assumption, which is architecture-dependent. We will compare the different sampling strategies described above in different numerical experiments in Section 3. The batch sizes  $B_m \leq \dots \leq B_1$  are defined through a geometric progression of the form  $B_i = \delta B_{i+1} = \delta^{m-i} B_m$ , where the batch size  $B_m$  at the last level and the multiplier  $\delta > 1$  are prescribed manually.

**Sampling strategy.** Data sampling is handled through a batcher providing the data structure  $\mathcal{B} = [\mathcal{B}^1, \dots, \mathcal{B}^{N_i/B_i}]$ , implemented as a list of  $N_i/B_i$  batch objects for  $1 \leq i \leq m$ . Each batch

$\mathcal{B}^k = [\mathcal{B}_1^k, \dots, \mathcal{B}_m^k]$  is itself a list of length  $m$ , where  $\mathcal{B}_i^k$  represents the set of data indices at correction level  $i$  and resolution  $R_i$ . The first element of the batch, i.e.,  $\mathcal{B}_1^k$ , is a set of  $B_1$  indices of coarse data sampled uniformly from  $\mathcal{N}_1$ . We explore two strategies to select the finer data indices within the  $k$ -th level of the batch:

- *Random sampling.* We uniformly sample  $\mathcal{B}_2^k, \dots, \mathcal{B}_m^k$  from the datasets  $\mathcal{N}_2, \dots, \mathcal{N}_m$ . This is a standard multi-level Monte Carlo sampling and ensures independence of the data samples across levels in the telescopic sum given by Eq. (3).
- *Nested sub-sampling.* To increase computational efficiency, data indices are sampled uniformly from the previous level in the resolution hierarchy as  $\mathcal{B}_i^k \subset \mathcal{B}_{i-1}^k$ , for  $2 \leq i \leq m$ . In contrast to random sampling, nested sub-sampling does not produce independent samples at each level. This sampling strategy can be viewed as a Multi-Level Quasi-Monte Carlo method (cf. Remark 2.2). We repeat the sampling procedure at every epoch to ensure full coverage of the data.

Fig. 6 in Appendix A.1 illustrates the two different sampling methods, where the finer data indices are uniformly samples from the original dataset (left), or sub-sampled from the previous resolution indices with the nested sub-sampling technique (right).

**Multi-resolution data batcher.** To preserve the computational efficiency of MLMC, we implement a cache-aware data management and loss computation system that optimizing memory transfers between host and device. Following Algorithm 1, the data batcher pre-loads the batch structures  $\mathcal{B}^k$  onto GPU memory at the beginning of each epoch and implements a resolution-aware memory manager that maintains a memory layout for tensors across resolution levels, facilitating efficient correction term computations. This approach achieves up to  $\mathcal{O}(m)$  reduction in transfer overhead compared to naive implementations, while maintaining a bounded GPU memory usage of  $\mathcal{O}(\sum_{i=1}^m B_i R_i^d)$ .

### 2.3 MLMC optimization algorithm

Our MLMC optimization algorithm is described in Algorithm 1 and implements the mini-batch strategies introduced in Section 2.2, along with the telescopic sum evaluation of the gradient given by Eq. (3). At a given gradient correction level  $2 \leq i \leq m$ , the loss is evaluated on samples  $(a_{i,j}, u_{i,j})$  from the batch  $\mathcal{B}_i^k$  of the observation set  $\mathcal{N}_i$  at resolution  $R_i$ . We then subtract the loss value at the same samples but coarsened to resolution  $R_{i-1}$ . The set of corresponding coarsen samples is denoted by  $\tilde{\mathcal{N}}_{i-1}$ . Note that it is essential to maintain consistency between the samples at different resolutions within a given correction level  $i$  when constructing the data batcher, in order to preserve the validity of the MLMC estimator. Once the gradient has been computed, any gradient-based optimization algorithm can be used to update the parameters of the neural operator, such as Adam [Kingma and Ba, 2015].

---

#### Algorithm 1 MLMC optimization algorithm

---

- 1: **Input:** Number of levels  $m$ , observations  $\mathcal{N}_i = \{(a_{i,j}, u_{i,j})\}_{j=1}^{N_i}$  at resolution  $R_i$ , batches  $\mathcal{B}_i^k$ , batch sizes  $B_i$ , sampling strategy, number of epochs  $n_e$ , optimizer
  - 2: **Output:**  $\theta^*$
  - 3: Initialize  $\theta_0$
  - 4: Initialize batcher
  - 5: **for**  $e$  in  $n_e$  **do**
  - 6:    $\mathcal{B} = \text{batcher.sample}(m, \mathcal{N}_i, B_i, \text{sampling strategy})$
  - 7:   **for**  $\mathcal{B}^k$  in  $\mathcal{B}$  **do**
  - 8:      $\text{total\_loss} = \text{loss}(\mathcal{N}_1, \mathcal{B}_1^k)$
  - 9:     **for**  $i$  in  $\{2, \dots, m\}$  **do**
  - 10:       $\text{total\_loss} += \text{loss}(\mathcal{N}_i, \mathcal{B}_i^k) - \text{loss}(\tilde{\mathcal{N}}_{i-1}, \mathcal{B}_{i-1}^k)$
  - 11:     **end for**
  - 12:      $\text{gradient} = \text{total\_loss.backward}()$
  - 13:   **end for**
  - 14:    $\text{optimizer.step}()$
  - 15: **end for**
-

### 3 Numerical experiments

We evaluate the efficiency MLMC training algorithm for neural operators on four state-of-the-art architectures: (i) Fourier neural operator (FNO) [Li et al., 2021b], (ii) message passing neural PDE solver (MP-PDE) [Brandstetter et al., 2022], and (iii) geometry-informed neural operator transformer (GINOT) [Liu et al., 2025]. Additional experiments with (iv) mesh-free convolutional neural network [Zakariaei et al., 2025] are presented in Appendix C.1. The test-cases considered in this work consist of standard (time-dependent) nonlinear PDE problems which are summarized in Appendix B, and include a fluid flow past a cylinder, and a complex 3D jet engine brackets dataset [Hong et al., 2024]. Note that the aim of this work is *not* to introduce new architectures, but rather improve the computational cost/accuracy trade-off in operator learning through MLMC training. All experiments are repeated on three random seeds and the results are averaged. The simulations are performed on a single Nvidia A100 GPU with 80GB of RAM.

#### 3.1 Fourier neural operator

FNOs are a family of neural operators that exploit spectral (Fourier) discretizations of the input and output functions [Li et al., 2021b]. These neural operators accept data at different resolutions using projection onto a latent dimension of fewer Fourier modes, which are then processed by Fourier convolutions. The MLMC training procedure introduced in Section 2 decreases the computational cost of the initial and final spectral convolutional layers and allows us to use fewer high-resolution data. This may be critical in large-scale applications where the cost of data acquisition might be high.

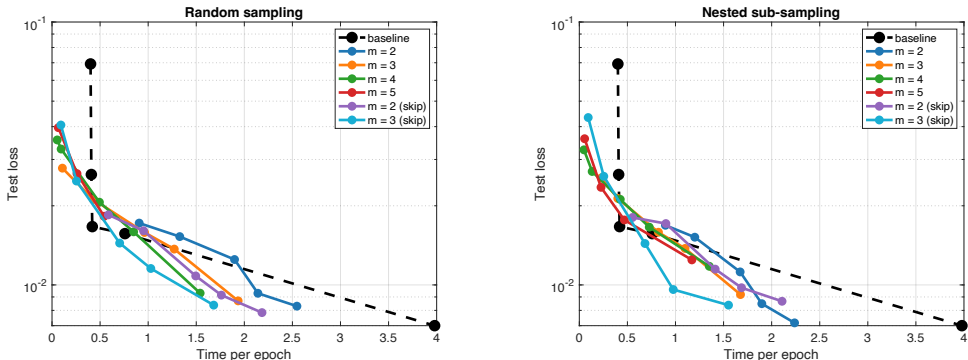


Figure 1: *Darcy test problem*. Final test loss against the average computational training time per epoch. The baseline plotted as a dotted black line reports the standard FNO performance when trained on increasing data resolutions, while the colored lines highlight a “Pareto curve” of MLMC accuracy/training time trade-off when varying the number of levels  $m$  and sampling factor  $\delta$ .

**Darcy flow problem.** We begin by training a two-dimensional FNO to learn the nonlinear diffusion coefficient field to solution operator associated with the standard Darcy flow problem introduced in [Li et al., 2021b]. To ensure fairness of the experiments, we keep the same hyper-parameters employed in the code released by [Li et al., 2021b], and train the original FNO at different resolutions, which we refer to as the baseline below. We report in Fig. 1 the final test accuracy against average (over 500 epochs) computational training time per epoch of the standard FNO baseline as the data resolution increases from  $15 \times 15$  to  $\{30 \times 30, 60 \times 60, 120 \times 120, 241 \times 241\}$ . We compare the results with the “Pareto curve” for different correction levels  $m \in \{2, 3, 4, 5\}$ , resulting from MLMC training with decreasing sampling multiplier factor  $\delta \in \{8, 4, 2, 1.5, 1\}$ . As  $\delta$  decreases, a higher number of fine-resolution data are used, which increases the accuracy but also the computational time. The proposed MLMC training algorithm enables us to reach almost the same testing accuracy achieved by traditional training at  $R = 241$ , while requiring only 60% of the training time. For completeness, we also report the tests referred to as “skip” in which the resolution scaling factor is 4 (instead of 2), and the considered resolutions are  $15 \times 15, 60 \times 60,$  and  $241 \times 241$ , as well as the nested sub-sampling strategy in Fig. 1 (right). In this way, we further increase the computational performance by reducing the total amount of fine samples required. Additional details about the dataset and numerical results are available in Appendices B.1 and C.2.

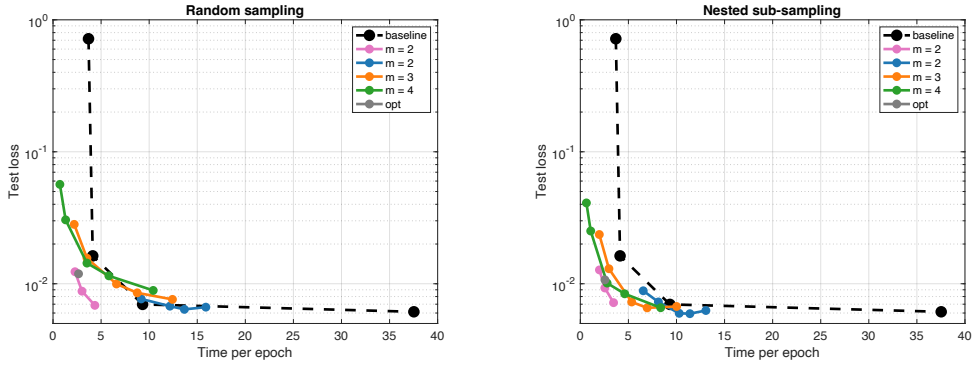


Figure 2: *Navier-Stokes problem*. Same as Fig. 1 with a FNO-3d trained on the time-dependent Navier-Stokes equations at increasing mesh resolutions  $8 \times 8$ ,  $16 \times 16$ ,  $32 \times 32$ ,  $64 \times 64$  (baseline) or with MLMC. The trained models are evaluated on a distinct test set at the finest resolution  $64 \times 64$ . The magenta curve corresponds to MLMC at finest level  $32 \times 32$  and coarsest level  $16 \times 16$  with decreasing  $\delta$ , and yields a better cost/accuracy trade-off compared to the baseline.

**Time-dependent Navier-Stokes equations.** We then consider the approximation of the time-forward solution operator associated to the Navier-Stokes equations (see Appendix B.3) using a 3D Fourier neural operator (FNO-3d) that directly convolves in space-time. Also here, we employ the same hyper-parameters employed in the code released by [Li et al., 2021b]. In Fig. 2, we display the Pareto frontier, in terms of average epoch training time and final testing loss, obtained by considering the standard FNO-3d training at different mesh resolutions (the baseline), and MLMC training with the two sampling strategies considered. Focusing on the baselines, we note that the testing loss values obtained at training resolutions  $32 \times 32$  and  $64 \times 64$  are very similar. Following this observation, we apply MLMC training with  $m = 2$  levels at finest resolution of  $32 \times 32$  and coarsest resolution of  $16 \times 16$ , while decreasing the sampling factor  $\delta$  from 8, 4, 2. The result is illustrated as a magenta curve in Fig. 2, and yields the best trade-off in terms of accuracy versus computational training time. Surprisingly, it allows us to maintain the accuracy reached by the baseline at the resolution  $R = 64$ , while decreasing the training time by a factor of 11 (resp. 3) compared to the baseline trained on a  $64 \times 64$  (resp.  $32 \times 32$ ) grid. We also considered the optimal sample allocation  $N_i^* = 4^{3i/2} N_3$  for  $i \in \{1, 2\}$  (predicted by the theory) with  $\delta^* = 2$ ,  $N_3^* = 45$  at resolution  $32 \times 32$ , and plotted as a grey dot in Fig. 2. Finally, we do not observe a significant difference in terms of accuracy when considering nested sub-sampling over random sampling. Now considering Fig. 3(left), we compare ground truth solutions with the approximations obtained by MLMC training algorithm with  $m = 4$  (resp.  $m = 2$ ) levels and  $\delta = 4$  (resp.  $\delta = 2$ ) at the time  $T = 40$ . Fig. 3 displays the evolution of the coarse and pairwise difference training losses composing the telescopic sum in Eq. (2) before evaluating the gradients for  $m = 4$  levels and  $\delta = 2$ . As expected, the coarse loss is dominating the telescopic sum throughout the training, while the pairwise difference losses across levels decreases with the level. We note a very small contribution from the last level, explaining the improved performance of the magenta curve settings (maximum resolution of  $32 \times 32$ ) in Fig. 2.

### 3.2 Message passing neural PDE solver

In this experiment, we consider the message-passing neural PDE solver architecture introduced by Brandstetter et al. [2022]. This is a type of graph neural network [Kipf and Welling, 2016, Battaglia et al., 2018] written in the encoder-processor-decoder framework following earlier works [Battaglia et al., 2018, Sanchez-Gonzalez et al., 2020]. We consider the problem of learning the time-forward velocity map  $u(\mathbf{x}, t) \mapsto u(\mathbf{x}, t + \Delta t)$  associated with the Navier-Stokes equations on a classical fluid flow past a cylinder problem, near the Hopf bifurcation at Reynolds number  $\text{Re} = 200$ , which features von Kármán vortex street patterns (see Appendix B.4). We generate four meshes  $M_4, \dots, M_1$  with decreasing mesh resolution using the Gmsh meshing software [Geuzaine and Remacle, 2009], and solve the corresponding time-dependent equations by means of finite elements and Crank-Nicolson time-stepping scheme using the Firedrake library [Rathgeber et al., 2016] on each mesh. This contrasts with previous experiments of Section 3.1 (and what is usually done in operator learning), where the numerical solutions are acquired on the finest resolution and down-sampled to coarser

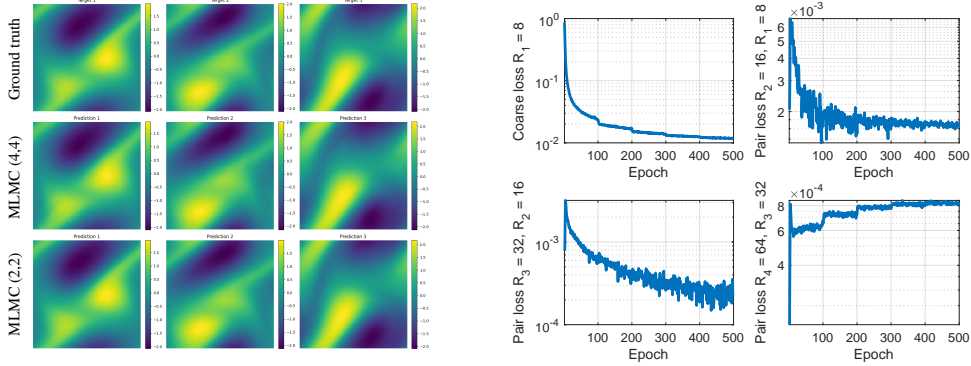


Figure 3: *Navier-Stokes problem*. Left: Comparison between the ground truth data (1st row), and the MLMC predicted solutions at  $t = 40$  with  $(m, \delta) = (4, 4)$  (2nd row) and  $(2, 2)$  (3rd row) for three different initial conditions. Right: Evolution of the coarse loss at the lowest resolution during training (top-left) and the pair losses in the telescopic sum expansion of the fine loss with  $\delta = 2$ .

ones. Here, we aim to evaluate the performance of MLMC training in the challenging settings where the coarse data quality is low (since they are generated by a numerical solver on a coarser spatial discretization).

Table 1: *Fluid flow past cylinder problem*. Baselines average training time per epoch and test loss when training the graph neural network for varying resolutions  $R_i$ , along with the results using MLMC training. Best trade-off, defined as training time multiplied by test MSE, is in **bold**, while second best is underlined.

Training resolution	$M_1$	$M_2$	$M_3$	$M_4$	MLMC (4,2)	MLMC (2,2)
Training epoch time [s]	0.36	0.67	1.50	1.84	0.66	0.85
MSE test loss [ $\times 10^{-2}$ ]	5.0	5.3	5.7	0.5	<u>1.1</u>	<b>0.8</b>

We report in Table 1 the mean square error (MSE) of the testing loss on the finest mesh  $M_4$  after training the MP-PDE graph neural networks on the different mesh resolutions. As expected, the testing error decreases as the training data resolution increases, but at the cost of increasing the computational training time. The last two columns of Table 1 report the test loss and average epoch training time (over 200 epochs) when using MLMC with  $m = 4$  levels and  $m = 2$  (with resolution  $M_4$  and  $M_1$  only), respectively, both with  $\delta = 2$ . We observe that the two MLMC training strategies yield the best trade-off in terms of accuracy versus computational time (measured by the product of the test loss and timings), outperforming the Pareto curve defined by the baseline performance.

### 3.3 Geometry-informed neural operator transformer

GINOT [Liu et al., 2025] is a neural operator architecture based on transformer networks Vaswani et al. [2017] that is designed to learn mappings between complex geometries (represented as CAD meshes or cloud of points) to corresponding solution fields (see Fig. 4). It consists of two main components: a geometry encoder and a solution decoder, which are combined by the cross-attention mechanism of the transformer network.

In this numerical experiment, we apply the MLMC neural operator training algorithm to the GINOT architecture on the complex DeepJEB dataset [Hong et al., 2024] containing 3D large-scale jet engine brackets and corresponding von Mises stress fields under

Table 2: Testing loss achieved by training GINOT on the coarse, fine, and test resolutions along with the corresponding average training time per epoch (over 500 epochs). The last row reports the performance of the MLMC training algorithm with  $m = 2$  levels of resolution  $R_1$  and  $R_2$  and a batch multiplier  $\delta = 2$ .

Training method	Test loss on $R_{\text{test}}$	Training epoch time [s]
Coarse resolution $R_1$	33.4%	16.9
Fine resolution $R_2$	22.7%	40.2
Test resolution $R_{\text{test}}$	18.6%	101.2
MLMC on $R_1 + R_2$	26.3%	20.1

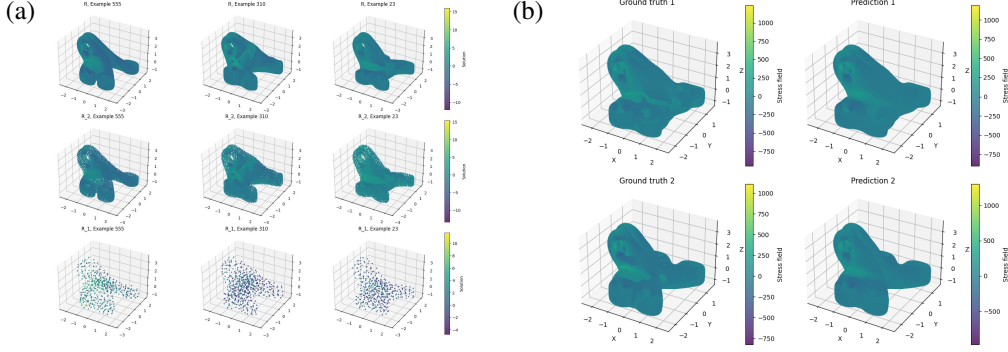


Figure 4: *DeepJEB test problem*. (a) Three sample geometries from the DeepJEB dataset at resolution  $R_{\text{test}}$ ,  $R_2$ , and  $R_1$ . (b) Comparison between the ground truth data (first column), and the MLMC solutions (second column) for different shapes.

vertical loading. The original dataset consists of sample geometries with resolutions ranging from  $R_{\text{test}} \in [18085, 55009]$ , referred to as the testing resolution (as used in Liu et al. [2025]). To enable MLMC training, we downsample the data to  $R_2 \in [4521, 13752]$  and  $R_1 \in [282, 859]$ , which we use as the fine and coarse resolutions, respectively. Further details on the dataset are available in Appendix B.5. Sample geometries from the dataset at different resolutions are depicted in Fig. 4(a). We train the GINOT on the DeepJEB dataset at different resolutions  $R_1$ ,  $R_2$ , and  $R_{\text{test}}$  over 500 epochs and report the average training time per epoch along with the test loss on the resolution  $R_{\text{test}}$  in Table 2. We note that we slightly modified the GINOT architecture and were able to outperform the testing error of 35.6% on the resolution  $R_{\text{test}}$  reported by Liu et al. [2025].

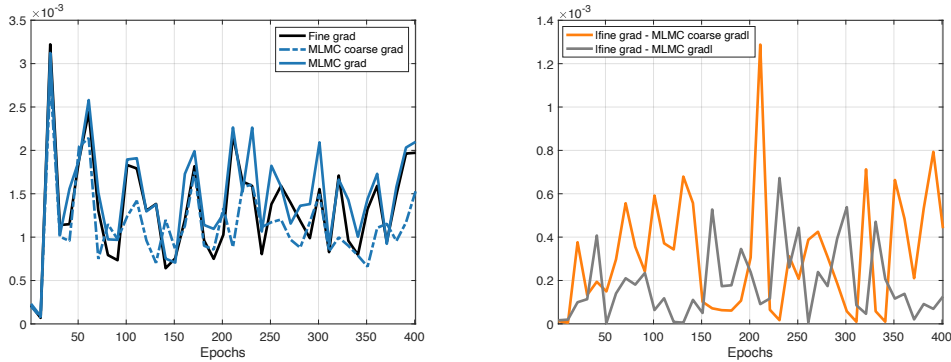


Figure 5: *DeepJEB test problem*. Left: Comparison between the norm of the fine gradients, the norm of the MLMC coarse gradients and MLMC gradients approximation over the same batch. Right: Absolute error between the fine gradients, and the gradients of the coarse and telescopic sum given by Eq. (3) over the same batch.

In the last row of Table 2, we show the performance (on the finest resolution  $R_{\text{test}}$ ) of the MLMC training algorithm with the two levels of resolution  $R_1$  and  $R_2$ , together with the corresponding computational training time per epoch. In this complex task, the proposed MLMC approach achieves a testing loss of 26.3% with a training time of 20.1 seconds per epoch, which improves upon the Pareto frontier of the training time/accuracy trade-off, between the coarse ( $R_1$ ) and fine ( $R_2$ ) resolution training baselines. We note that the training time is nearly halved compared to the fine resolution training without losing too much accuracy. In Fig. 4(b), we display one ground truth sample at resolution  $R_{\text{test}}$  and its MLMC approximation obtained by considering two levels of resolutions  $m = 2$ , with a nested sub-sampling as pairing strategy, 1723 and 213 samples at level one and two (optimal sample progression), and a batch multiplier of  $\delta = 2$ . Finally, in Fig. 5, we display the corresponding approximation of the fine gradients as we include the fine resolution correction term in the telescopic sum of Eq. (3).

## 4 Conclusions

Neural operators have shown remarkable promise in the approximation of operators associated with PDEs, but their practical adoption is hindered by the computational cost of high-resolution training. We introduced a mathematically rigorous MLMC approach to efficiently train neural operators by approximating fine-resolution gradients through a telescopic sum formulation across mesh hierarchies or function discretizations. Our implementation is characterized by a careful design of resolution-aware data structures and optimized memory management. Our numerical results, across a variety of state-of-the-art neural operator architectures and complex benchmarks, demonstrated that the proposed MLMC training algorithm accelerates training by up to 60%.

Current limitations, that can be addressed by future developments, are related to the need of sufficiently complex model architecture in order to benefit from the multi-resolution approach. The optimal sampling distribution depends on problem-specific variance decay rates that may need fine-tuning for each application. Finally, approximation errors from coarse representations might be dominating in problems with extremely sharp features or discontinuities, and potentially reduce the efficiency of the MLMC approach. Additional future developments could include dynamically adjusting the sampling distributions across resolutions during training. Finally, MLMC is a flexible approach, which leads itself to pretraining and finetuning applications, and possibly extensions to online learning scenarios, thus enabling efficient adaptation of pre-trained models to new data distributions with minimal computational overhead.

## Acknowledgments and Disclosure of Funding

This work originates from an Oberwolfach workshop on Deep Learning for PDE-based Inverse Problems. SF is member of the Gruppo Nazionale Calcolo Scientifico-Istituto Nazionale di Alta Matematica (GNCS-INdAM) and acknowledges the project “Dipartimento di Eccellenza” 2023–2027, funded by MUR. SF acknowledges the Istituto Nazionale di Alta Matematica (INdAM) for the financial support received (Scholarships for visiting periods abroad, 2023–2024) and the project FAIR (Future Artificial Intelligence Research), funded by the NextGenerationEU program within the PNRR-PE-AI scheme (M4C2, Investment 1.3, Line on Artificial Intelligence). CBS and SF acknowledge the EPSRC program grant in “The Mathematics of Deep Learning”, under the project EP/V026259/1. NB was supported by the Office of Naval Research (ONR), under grant N00014-23-1-2729.

## References

- Anima Anandkumar, Kamyar Azizzadenesheli, Kaushik Bhattacharya, Nikola Kovachki, Zongyi Li, Burigede Liu, and Andrew Stuart. Neural operator: Graph kernel network for partial differential equations. In *ICLR 2020 workshop on integration of deep neural models and differential equations*, 2020.
- Peter W Battaglia, Jessica B Hamrick, Victor Bapst, Alvaro Sanchez-Gonzalez, Vinicius Zambaldi, Mateusz Malinowski, Andrea Tacchetti, David Raposo, Adam Santoro, Ryan Faulkner, et al. Relational inductive biases, deep learning, and graph networks. *arXiv preprint arXiv:1806.01261*, 2018.
- Nicolas Boullé and Alex Townsend. A mathematical guide to operator learning. In *Handbook of Numerical Analysis*, volume 25, pages 83–125. Elsevier, 2024.
- Nacime Bouziani and Nicolas Boullé. Structure-preserving operator learning. *arXiv preprint arXiv:2410.01065*, 2024.
- Johannes Brandstetter, Daniel E Worrall, and Max Welling. Message Passing Neural PDE Solvers. In *International Conference on Learning Representations*, 2022.
- Susanne C Brenner and Ridgway L Scott. *The mathematical theory of finite element methods*. Springer, 2008.
- Shuhao Cao. Choose a transformer: Fourier or Galerkin. *Advances in Neural Information Processing Systems*, 34:24924–24940, 2021.

- K Andrew Cliffe, Michael B Giles, Robert Scheichl, and Aretha L Teckentrup. Multilevel Monte Carlo methods and applications to elliptic PDEs with random coefficients. *Comput. Vis. Sci.*, 14: 3–15, 2011.
- Luca Dede’ and Alfio Quarteroni. Optimal control and numerical adaptivity for advection-diffusion equations. *ESAIM: Math. Model. Numer. Anal.*, 39(5):1019–1040, 2005.
- Matthias Fey and Jan Eric Lenssen. Fast graph representation learning with PyTorch Geometric. *arXiv preprint arXiv:1903.02428*, 2019.
- Eshed Gal, Moshe Eliasof, Carola-Bibiane Schönlieb, Eldad Haber, and Eran Treister. Towards efficient training of graph neural networks: A multiscale approach. *arXiv preprint arXiv:2503.19666*, 2025.
- Christophe Geuzaine and Jean-François Remacle. Gmsh: A 3-D finite element mesh generator with built-in pre-and post-processing facilities. *International journal for numerical methods in engineering*, 79(11):1309–1331, 2009.
- Michael B Giles. Multilevel monte carlo path simulation. *Oper. Res.*, 56(3):607–617, 2008.
- Michael B Giles. Multilevel Monte Carlo Methods. *Acta Numer.*, 24:259–328, 2015.
- Michael B Giles and Benjamin J Waterhouse. Multilevel quasi-Monte Carlo path simulation. In *Advanced Financial Modelling*, pages 165–182. De Gruyter, 2009.
- Abdul-Lateef Haji-Ali, Fabio Nobile, Erik von Schwerin, and Raúl Tempone. Optimization of mesh hierarchies in multilevel Monte Carlo samplers. *Stoch. Partial Differ. Equ.: Anal. Comput.*, 4(1): 76–112, 2016.
- Zhongkai Hao, Zhengyi Wang, Hang Su, Chengyang Ying, Yinpeng Dong, Songming Liu, Ze Cheng, Jian Song, and Jun Zhu. Gnot: A general neural operator transformer for operator learning. In *International Conference on Machine Learning*, pages 12556–12569. PMLR, 2023.
- Juncai He, Xinliang Liu, and Jinchao Xu. MgNO: Efficient Parameterization of Linear Operators via Multigrid. In *International Conference on Learning Representations*, 2024.
- Seongjun Hong, Yongmin Kwon, Dongju Shin, Jangseop Park, and Namwoo Kang. Deepjeb: 3d deep learning-based synthetic jet engine bracket dataset. *Journal of Mechanical Design*, 147(4): 041703, 2024.
- Jikai Jin, Yiping Lu, Jose Blanchet, and Lexing Ying. Minimax optimal kernel operator learning via multilevel training. In *International Conference on Learning Representations*, 2023.
- Diederik P Kingma and Jimmy Ba. Adam: A method for stochastic optimization. In *International Conference on Learning Representations*, 2015.
- Thomas N Kipf and Max Welling. Semi-supervised classification with graph convolutional networks. *arXiv preprint arXiv:1609.02907*, 2016.
- Nikola Kovachki, Samuel Lanthaler, and Siddhartha Mishra. On universal approximation and error bounds for Fourier neural operators. *J. Mach. Learn. Res.*, 22(290):1–76, 2021.
- Nikola Kovachki, Zongyi Li, Burigede Liu, Kamyar Azizzadenesheli, Kaushik Bhattacharya, Andrew Stuart, and Anima Anandkumar. Neural operator: Learning maps between function spaces with applications to PDEs. *J. Mach. Learn. Res.*, 24(89):1–97, 2023.
- Nikola B Kovachki, Samuel Lanthaler, and Andrew M Stuart. Operator learning: Algorithms and analysis. In *Handbook of Numerical Analysis*, volume 25, pages 419–467. Elsevier, 2024.
- Frances Y Kuo, Christoph Schwab, and Ian H Sloan. Quasi-Monte Carlo finite element methods for a class of elliptic partial differential equations with random coefficients. *SIAM J. Numer. Anal.*, 50(6):3351–3374, 2012.

- Frances Y Kuo, Christoph Schwab, and Ian H Sloan. Multi-level quasi-Monte Carlo finite element methods for a class of elliptic PDEs with random coefficients. *Found. Comput. Math.*, 15:411–449, 2015.
- Samuel Lanthaler, Siddhartha Mishra, and George E Karniadakis. Error estimates for deepONets: A deep learning framework in infinite dimensions. *Trans. Math. Appl.*, 6(1):tnac001, 2022.
- Zhihan Li, Yuwei Fan, and Lexing Ying. Multilevel fine-tuning: Closing generalization gaps in approximation of solution maps under a limited budget for training data. *Multiscale Model. Simul.*, 19(1):344–373, 2021a.
- Zongyi Li, Nikola Kovachki, Kamyar Azizzadenesheli, Burigede Liu, Andrew Stuart, Kaushik Bhattacharya, and Anima Anandkumar. Multipole graph neural operator for parametric partial differential equations. *Advances in Neural Information Processing Systems*, 33:6755–6766, 2020.
- Zongyi Li, Nikola Borislavov Kovachki, Kamyar Azizzadenesheli, Burigede liu, Kaushik Bhattacharya, Andrew Stuart, and Anima Anandkumar. Fourier Neural Operator for Parametric Partial Differential Equations. In *International Conference on Learning Representations*, 2021b.
- Qibang Liu, Vincient Zhong, Hadi Meidani, Diab Abueidda, Seid Koric, and Philippe Geubelle. Geometry-Informed Neural Operator Transformer. *arXiv preprint arXiv:2504.19452*, 2025.
- Lu Lu, Pengzhan Jin, Guofei Pang, Zhongqiang Zhang, and George Em Karniadakis. Learning nonlinear operators via DeepONet based on the universal approximation theorem of operators. *Nat. Mach. Intell.*, 3(3):218–229, 2021.
- Kjetil O Lye, Siddhartha Mishra, and Roberto Molinaro. A multi-level procedure for enhancing accuracy of machine learning algorithms. *Eur. J. Appl. Math.*, 32(3):436–469, 2021.
- Tobias Pfaff, Meire Fortunato, Alvaro Sanchez-Gonzalez, and Peter Battaglia. Learning mesh-based simulation with graph networks. In *International Conference on Learning Representations*, 2020.
- Charles Ruizhongtai Qi, Li Yi, Hao Su, and Leonidas J Guibas. Pointnet++: Deep hierarchical feature learning on point sets in a metric space. *Advances in Neural Information Processing Systems*, 30, 2017.
- Florian Rathgeber, David A Ham, Lawrence Mitchell, Michael Lange, Fabio Luporini, Andrew TT McRae, Gheorghe-Teodor Bercea, Graham R Markall, and Paul HJ Kelly. Firedrake: automating the finite element method by composing abstractions. *ACM Trans. Math. Softw.*, 43(3):1–27, 2016.
- Lars Ruthotto and Eldad Haber. Deep neural networks motivated by partial differential equations. *J. Math. Imaging Vis.*, 62:352–364, 2020.
- Alvaro Sanchez-Gonzalez, Jonathan Godwin, Tobias Pfaff, Rex Ying, Jure Leskovec, and Peter Battaglia. Learning to simulate complex physics with graph networks. In *International conference on machine learning*, pages 8459–8468. PMLR, 2020.
- Michael Schäfer and Stefan Turek. Benchmark computations of laminar flow around a cylinder. In *Flow Simulation with High-Performance Computers II*, pages 547–566. Springer, 1996.
- C. Taylor and P. Hood. A numerical solution of the Navier-Stokes equations using the finite element technique. *Comput. Fluids*, 1(1):73–100, 1973.
- Ashish Vaswani, Noam Shazeer, Niki Parmar, Jakob Uszkoreit, Llion Jones, Aidan N Gomez, Łukasz Kaiser, and Illia Polosukhin. Attention is all you need. *Advances in Neural Information Processing Systems*, 30, 2017.
- Eamon Whalen, Azariah Beyene, and Caitlin Mueller. SimJEB: Simulated jet engine bracket dataset. *Computer Graphics Forum*, 40(5):9–17, 2021.
- Niloufar Zakariaei, Shadab Ahamed, Eldad Haber, and Moshe Eliasof. Multiscale training of convolutional neural networks. *arXiv preprint arXiv:2501.12739*, 2025.

# Appendix

## A Additional technical details

We begin by verifying the assumptions of the dominated convergence theorem to move the gradient inside the expectation in Eq. (1).

**Dominated convergence theorem for Bochner integral.** Under suitable smoothness assumption on the architecture of  $\mathcal{G}_\theta$ , namely that it is differentiable with respect to  $\theta$  and that  $\nabla_{\theta_i} \mathcal{G}_\theta \in L^2_\mu(\mathcal{A}; \mathcal{U})$ , for all  $1 \leq i \leq p$ , if  $a \sim \mu$  we have

$$|\nabla_{\theta_i} \|\mathcal{G}^\dagger(a) - \mathcal{G}_\theta(a)\|_{\mathcal{U}}^2| = 2|\langle \mathcal{G}^\dagger(a) - \mathcal{G}_\theta(a), \nabla_{\theta_i} \mathcal{G}_\theta(a) \rangle_{\mathcal{U}}| \leq 2\|\mathcal{G}^\dagger(a) - \mathcal{G}_\theta(a)\|_{\mathcal{U}} \|\nabla_{\theta_i} \mathcal{G}_\theta(a)\|_{\mathcal{U}}.$$

Following Cauchy–Schwarz inequality, we can bound the expectation of the gradient as

$$\mathbb{E}_{a \sim \mu} [\|\nabla_{\theta_i} \|\mathcal{G}^\dagger(a) - \mathcal{G}_\theta(a)\|_{\mathcal{U}}^2] \leq 2\|\mathcal{G}^\dagger - \mathcal{G}_\theta\|_{L^2_\mu(\mathcal{A}; \mathcal{U})} \|\nabla_{\theta_i} \mathcal{G}_\theta\|_{L^2_\mu(\mathcal{A}; \mathcal{U})} < \infty.$$

We can then apply the dominated convergence theorem for Bochner integral and move the gradient inside the expectation in Eq. (1) to obtain

$$\nabla_\theta (\mathbb{E}_{a \sim \mu} \|\mathcal{G}^\dagger(a) - \mathcal{G}_\theta(a)\|_{\mathcal{U}}^2) = \mathbb{E}_{a \sim \mu} [\nabla_\theta \|\mathcal{G}^\dagger(a) - \mathcal{G}_\theta(a)\|_{\mathcal{U}}^2], \quad (4)$$

*Proof of Proposition 2.1.* Let  $1 \leq i \leq m$  be the level of the mesh, for a given  $a \sim \mu$ , we are interested in bounding the difference between the gradients on the coarse and fine meshes in Eq. (2). We assume that the operators  $\mathcal{G}^\dagger$ ,  $\mathcal{G}_\theta$  are Lipschitz continuous from  $L^2(\Omega_{\mathcal{A}}) \rightarrow \mathcal{U}$  and that  $\mu$  is compactly supported on  $H^k(\Omega_{\mathcal{A}})$  (see [Bouziani and Boullé, 2024]). Moreover, we assume that each component of  $\nabla_\theta \mathcal{G}_\theta$  (with respect to  $1 \leq s \leq p$ ) is Lipschitz continuous from  $L^2(\Omega_{\mathcal{A}}) \rightarrow \mathcal{U}$ , with constant  $L_\theta$ . We remark that  $X_\theta^i(a) = X_\theta(\mathcal{P}_i a)$ , and for  $a \sim \mu$  denote  $H_\theta(a) := \mathcal{G}^\dagger(a) - \mathcal{G}_\theta(a)$ . Since  $\mathcal{G}^\dagger$  and  $\mathcal{G}_\theta$  are Lipschitz continuous, the application  $H_\theta : L^2(\Omega_{\mathcal{A}}) \rightarrow \mathcal{U}$  is Lipschitz continuous with Lipschitz constant  $\text{Lip}(H_\theta) = \text{Lip}(\mathcal{G}^\dagger) + \text{Lip}(\mathcal{G}_\theta)$ . Let  $1 \leq s \leq p$  and  $a \sim \mu$ , then

$$\begin{aligned} |\nabla_{\theta_s} X_\theta(\mathcal{P}_i a) - \nabla_{\theta_s} X_\theta(a)| &= 2|\langle H_\theta(\mathcal{P}_i a), \nabla_{\theta_s} \mathcal{G}_\theta(\mathcal{P}_i a) \rangle - \langle H_\theta(a), \nabla_{\theta_s} \mathcal{G}_\theta(a) \rangle| \\ &\leq 2|\langle H_\theta(a), \nabla_{\theta_s} \mathcal{G}_\theta(a) - \nabla_{\theta_s} \mathcal{G}_\theta(\mathcal{P}_i a) \rangle| \\ &\quad + 2|\langle H_\theta(a) - H_\theta(\mathcal{P}_i a), \nabla_{\theta_s} \mathcal{G}_\theta(\mathcal{P}_i a) \rangle| \\ &\leq 2(L_\theta \|H_\theta(a)\|_{\mathcal{U}} + \text{Lip}(H_\theta) \|\nabla_{\theta_s} \mathcal{G}_\theta(\mathcal{P}_i a)\|_{\mathcal{U}}) \|a - \mathcal{P}_i a\|_{L^2(\Omega_{\mathcal{A}})} \\ &\leq C_\theta \|a - \mathcal{P}_i a\|_{L^2(\Omega_{\mathcal{A}})}, \end{aligned}$$

where we used the Cauchy-Schwarz inequality to obtain the second inequality, and introduced the constant  $C_\theta > 0$  to bound the first term in the second inequality uniformly over  $a$  because  $\mu$  is compactly supported on  $H^k(\Omega_{\mathcal{A}})$  and the operators are continuous. Here, we require that  $\nabla_\theta \mathcal{G}_\theta$ ,  $\mathcal{G}^\dagger$ , and  $\mathcal{G}_\theta$  are Lipschitz continuous, and use the fact that  $a$  belongs to a compact domain and  $H_\theta$ ,  $\nabla_\theta \mathcal{G}_\theta$  are continuous to bound the last two terms uniformly over  $a \sim \mu$ . While these are strong assumptions, they are standard in the operator learning approximation theory literature [Kovachki et al., 2021] and are necessary to control the image of the source term distribution through the nonlinear operator. Finally, we employ a standard finite element error estimate [Brenner and Scott, 2008, Eq. 4.4.28] to bound the difference between the projection  $\mathcal{P}_i a$  and the original function  $a$  as

$$\|\mathcal{P}_i a - a\|_{L^2(\Omega_{\mathcal{A}})} \leq C 2^{-ki} \|a\|_{H^k(\Omega_{\mathcal{A}})}.$$

Using the compactness of the measure  $\mu$ , we conclude that there exists a constant  $M_\theta > 0$  such that

$$\|\nabla_\theta X_\theta^i(a) - \nabla_\theta X_\theta(a)\|_2 \leq M_\theta 2^{-ki}. \quad (5)$$

Moreover, by triangular inequality, we have

$$\begin{aligned} \|\nabla_\theta X_\theta^i(a) - \nabla_\theta X_\theta^{i-1}(a)\|_2 &\leq \|\nabla_\theta X_\theta^i(a) - \nabla_\theta X_\theta(a)\|_2 + \|\nabla_\theta X_\theta^{i-1}(a) - \nabla_\theta X_\theta(a)\|_2 \\ &\leq 3M_\theta 2^{-ki} \end{aligned} \quad (6)$$

Combining Eqs. (5) and (6), we obtain the following bound for the expectation of the approximation of the gradient, and the variance of the multilevel estimator:

$$\mathbb{E}_{a \sim \mu} [\|\nabla_\theta X_\theta^i(a) - \nabla_\theta X_\theta(a)\|_2] \leq M_\theta 2^{-ki}, \quad \text{Var}_{a \sim \mu} [\|\nabla_\theta X_\theta^i(a) - \nabla_\theta X_\theta^{i-1}(a)\|_2] \leq \frac{9M_\theta^2}{4} 2^{-2ki}.$$

If one assumes that the computational cost  $C_i$  of the projection step in neural operators scales linearly with respect to the degrees of freedom of the finite element space  $\mathcal{A}_i$ , i.e.,  $C_i \leq ck^d 2^{di}$ . Then, following [Giles, 2015, Thm. 2.1], for any  $\epsilon > 0$ , there exists a number of level  $m$ , and optimal allocation of samples  $N_i \propto 2^{-(2k+d)i/2}$  per level such that the MLMC estimator given by Eq. (2) has a mean square error bounded by  $\epsilon^2$ .  $\square$

### A.1 Sampling strategies

We illustrate the random and nested sampling strategies in Fig. 6.

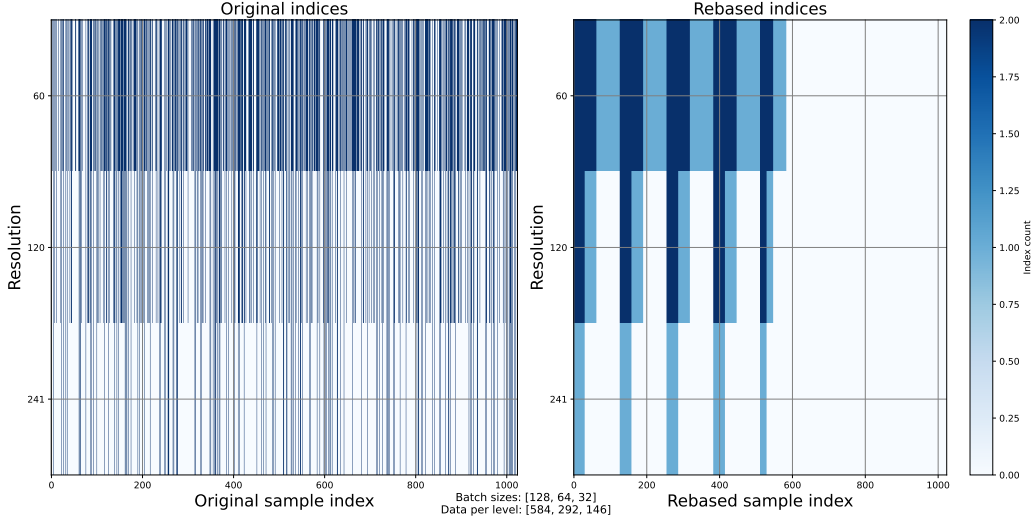


Figure 6: Illustration of random sampling (left) and nested sub-sampling (right) for  $m = 3$  levels.

## B Test problems

### B.1 Darcy Flow equation

We consider the steady state Darcy flow equation on the domain  $\Omega = [0, 1]^2$  as [Li et al., 2021b]:

$$\begin{aligned} -\nabla \cdot (a(\mathbf{x})\nabla u(\mathbf{x})) &= 1, & \mathbf{x} \in \Omega, \\ u(\mathbf{x}) &= 0, & \mathbf{x} \in \partial\Omega, \end{aligned} \quad (7)$$

where the diffusion coefficient  $a : \Omega \rightarrow \mathbb{R}$  is chosen such that  $a(\mathbf{x}) = \psi \circ \mu(\mathbf{x})$ , where  $\mu \sim \mathcal{N}(0, (-\Delta + 9I)^{-2})$  with zero Neumann boundary conditions on the Laplacian, and  $\psi : \mathbb{R} \rightarrow \mathbb{R}$  is defined as  $\psi(x) = 12$  if  $x \geq 0$  and 3 otherwise. We are interested in learning the nonlinear operator  $a \mapsto u$  mapping the diffusion operator  $a$  to the corresponding solution  $u$  to Eq. (7). The equation is solved numerically for  $N = 1024$  random diffusion coefficients on an equispaced  $241 \times 241$  grid using a second-order finite difference scheme, and downsampled to the lower resolutions such that  $\{R_i \times R_i\}_{i=1}^5 = \{241 \times 241, 120 \times 120, 60 \times 60, 30 \times 30, 15 \times 15\}$ .

### B.2 Advection-diffusion equation

We consider an advection-diffusion equation on a two-dimensional rectangle  $\Omega = [-5, 5] \times [-4, 4]$ :

$$\begin{aligned} -\nabla \cdot (\nu(\mathbf{x})\nabla u(\mathbf{x})) + \mathbf{b} \cdot \nabla u(\mathbf{x}) &= f(\mathbf{x}), & \mathbf{x} \in \Omega, \\ u(\mathbf{x}) &= 0, & \mathbf{x} \in \Gamma_D, \\ \nu \frac{\partial u}{\partial n} &= 0, & \mathbf{x} \in \Gamma_N. \end{aligned} \quad (8)$$

This equation models the transport and diffusion of the pollutant released by industrial chimneys into a plane [Dede' and Quarteroni, 2005]. Here,  $\mathbf{b} = (0.0025, 0.0025)^\top$ ,  $f(\mathbf{x}) = \sum_{i=1}^4 f_i \chi_{D_i}(\mathbf{x})$ , where  $f_i \geq 0$ , and  $D_i$  the spatial region representing the  $i$ -th chimney and  $f_i$  its emission rate (normalized with respect to an appropriate emission volume). We impose a homogeneous Dirichlet condition over the inflow boundary  $\Gamma_D = \{\mathbf{x} \in \partial\Omega : \mathbf{b} \cdot \mathbf{n}(\mathbf{x}) < 0\}$ , where  $\mathbf{n}(\mathbf{x})$  is the unit vector directed outward, and homogeneous Neumann condition on the outflow boundary  $\Gamma_N = \partial\Omega \setminus \Gamma_D$ . For the expression of the diffusion field  $\nu$  we refer to [Dede' and Quarteroni, 2005]. Eq. (8) is discretized in space using linear finite elements by considering  $\{R_i \times R_i\}_{i=1}^3 = \{300 \times 300, 150 \times 150, 75 \times 75\}$  space points. The dataset consists of  $N = 1024$  samples obtained by drawing instances of  $x_c^i \sim \mathcal{U}(-3, -2)$  and  $r^i \sim \mathcal{U}(0.1, 0.3)$ , parametrizing the regions  $D_i$ , for  $i \in \{1, \dots, 4\}$ .

### B.3 Navier-Stokes equations

The two-dimensional time-dependent Navier-Stokes equations are expressed in vorticity form on the unit torus as follows [Li et al., 2021b]:

$$\begin{aligned} \frac{\partial w(\mathbf{x}, t)}{\partial t} + \mathbf{u}(\mathbf{x}, t) \cdot \nabla w(\mathbf{x}) - \nu \Delta w(\mathbf{x}, t) &= f(\mathbf{x}, t), & (\mathbf{x}, t) \in (0, 1)^2 \times [0, T], \\ \nabla \cdot \mathbf{u}(\mathbf{x}, t) &= 0, & (\mathbf{x}, t) \in (0, 1)^2 \times [0, T], \\ w(\mathbf{x}, 0) &= w_0(\mathbf{x}), & \mathbf{x} \in (0, 1)^2, \end{aligned} \quad (9)$$

where  $\mathbf{u} : \Omega \times [0, T) \rightarrow \mathbb{R}^2$  is the velocity field and  $w = \nabla \times \mathbf{u}$  is the vorticity field. The initial condition for the vorticity field is generated as  $w_0 \sim \mathcal{N}(0, 7^{3/2}(-\Delta + 49I)^{-2.5})$ , the forcing term is given by  $f = 0.1(\sin(2\pi(x+y)) + \cos(2\pi(x+y)))$ , and the viscosity coefficient is equal to  $\nu = 10^{-3}$ . Eq. (9) are equipped with periodic boundary conditions. We are interested in learning the operator which maps the vorticity field up to time  $t = 10$  to the vorticity up to time  $T = 50$ . The equations are numerically solved by a pseudo-spectral method and a Crank-Nicolson time scheme for the viscous term with an explicit treatment of the nonlinear term on a uniform grid of resolution  $256 \times 256$ , and a time discretization step  $\Delta t = 10^{-4}$ . The dataset is generated by downsampling the solutions to  $\{R_i \times R_i\}_{i=1}^4 = \{64 \times 64, 32 \times 32, 16 \times 16, 8 \times 8\}$  space discretization points and storing them at every time units  $t \in \{1, \dots, 50\}$ . The number of samples of the initial conditions  $w_0$  and resulting trajectories is set to  $N = 3000$ .

### B.4 Fluid flow past a cylinder

We are interested in learning the time-forward operator associated with the classical cylinder flow test-case, a well-known benchmark problem for the evaluation of numerical algorithms for incompressible time-dependent Navier-Stokes equations [Schäfer and Turek, 1996]. The equations read as

$$\begin{aligned} \frac{\partial \mathbf{u}}{\partial t} + (\mathbf{u} \cdot \nabla) \mathbf{u} - \nabla \cdot \frac{2}{\text{Re}} \epsilon(\mathbf{u}) + \nabla p &= 0 & \text{in } \Omega \times (0, T], \\ \nabla \cdot \mathbf{u} &= 0 & \text{in } \Omega \times (0, T], \\ \mathbf{u}(\mathbf{x}, 0) &= \mathbf{u}_0(\mathbf{x}) & \mathbf{x} \in \Omega, \end{aligned} \quad (10)$$

where  $\Omega \subset \mathbb{R}^2$ ,  $T = 50$ ,  $p : \Omega \times [0, T) \rightarrow \mathbb{R}$  is the pressure field, the Reynolds number is  $\text{Re} = 200$ , and  $\epsilon(\mathbf{u}) = (\nabla \mathbf{u} + \nabla \mathbf{u}^\top)/2$ . The boundary conditions are defined as follows:  $\mathbf{u} = (1, 0)^\top$  on the upper and lower side of  $\Omega$ , a homogeneous Dirichlet boundary condition on the disk obstacle, and a "do-nothing" condition on the right side of the domain. We consider fluid fields including laminar flow as well as vortex structures. The dataset is formed of  $N = 200$  samples obtained by considering different random inflow conditions on the left boundary, which are split as 150 for training and the remaining 50 for testing. The equations are discretized in space using standard Taylor-Hood finite elements for velocity and pressure, which is a stable element pair for the Stokes equation [Taylor and Hood, 1973], and in time by a Crank-Nicolson time-stepping scheme with a timestep of 0.25. The velocity and pressure solutions are sampled every  $\Delta t = 1$  timesteps and we aim to learn the time-forward operator  $\mathbf{u}(\cdot, t) \mapsto \mathbf{u}(\cdot, t + \Delta t)$ , by mapping the first 30 time steps to the next 20. The finest mesh  $M_4$  on which the simulations are performed contains 14631 triangle elements with 7217 nodes, and a target element size of 0.03 near the obstacle and 0.12 on the boundary of the domain. The computed solutions are projected onto a space of linear finite elements and the values at the mesh nodes are saved. We also generated coarser meshes with approximately twice fewer nodes from level

$i + 1$  to level  $i$  (specifications are available in Table 3) to run the MLMC algorithm, and performed numerical simulations on these coarser meshes to acquire the corresponding data.

Table 3: Characteristics of the different meshes used in the fluid flow past a cylinder example.

Mesh name	# nodes	# elements	mesh size [obstacle]	mesh size [boundary]
$M_4$	7217	14631	0.05	0.18
$M_3$	3808	7760	0.07	0.25
$M_2$	1645	3387	0.10	0.4
$M_1$	806	1682	0.14	0.6

## B.5 Jet engine brackets

The Deep jet engine bracket (DeepJEB) dataset [Hong et al., 2024] is publicly accessible and comprises  $N = 2138$  samples of complex 3D jet engine brackets with arbitrary shapes and sizes. More precisely, the dataset was created using deep generative models to perform data augmentation on the simulated jet engine bracket (SimJEB) dataset [Whalen et al., 2021] thus enhancing the diversity of shapes and the performance features by means of AI. SimJEB is one of the largest publicly available dataset for jet engine bracket, and includes 381 hand-designed CAD models, along with finite element simulation results of von Mises stress and displacement fields under different loading conditions. Following [Liu et al., 2025], we focus on the approximation of the von Mises stress data under vertical loading. The DeepJEB dataset volume mesh nodes ranges from 18085 to 55009, which we refer to as testing resolution  $R_{\text{test}}$  in this paper and use to evaluate the super-resolution capabilities of the trained transformer model Liu et al. [2025]. To apply the MLMC training algorithm, we generate a similar dataset at a coarse level of resolution  $R_1 \in [282, 859]$  and a fine level of resolution  $R_2 \in [4521, 13752]$  by downsampling the original dataset. The dataset downsampling was performed using the PointNet++ [Qi et al., 2017] algorithm exploiting the `pool . fps` command from the `torch_geometric` library Fey and Lenssen [2019] with a default sampling ratio of 0.5. In the numerical experiments of Section 3.3, we consider the same hyperparameters as in [Liu et al., 2025] for the GINOT architecture, with the exception of the number of attention heads in the encoder and decoder, which we set to 4 instead of 1, encoder/decoder cross-attention layers (set to 4) and encoder self-attention layers (set to 4). By using a larger architecture, we are able to improve the performance of the GINOT model on the test resolution and reach a normalized mean square error of 18.6%, which is much lower than 35.6% reported in [Liu et al., 2025].

## C Details of numerical experiments

### C.1 Mesh-free convolutional neural network

The architecture considered is a resolution-invariant CNN specifically designed for mesh-based inputs, introduced in [Zakariaei et al., 2025, Ruthotto and Haber, 2020]. The main idea is to define convolution operations without relying on a mesh of the domain  $\Omega \subset \mathbb{R}^2$ , adopting a mesh-free approach instead. More precisely, the mesh-free convolution reads as

$$C(\boldsymbol{\xi}) * a(\mathbf{x}) = (\gamma_0 + [\gamma_x, \gamma_y]^T \nabla) \tilde{v}(\tau, \mathbf{x}), \quad (11)$$

where  $\tilde{v}(\tau, \mathbf{x})$  is obtained by the solution of the following parabolic PDE

$$\begin{cases} \frac{\partial \tilde{v}(t, \mathbf{x})}{\partial t} = \mathcal{L}(\boldsymbol{\alpha}) \tilde{v}(t, \mathbf{x}) & t \in (0, \tau], \\ \tilde{v}(0, \mathbf{x}) = \mathcal{R}(\boldsymbol{\theta}) a(\mathbf{x}). \end{cases} \quad (12)$$

The elliptic differential operator in Eq. (12) is defined as

$$\mathcal{L}(\boldsymbol{\alpha}) = \alpha_{xx} \frac{\partial^2 v}{\partial x^2} + 2\alpha_{xy} \frac{\partial^2 v}{\partial x \partial y} + \alpha_{yy} \frac{\partial^2 v}{\partial y^2},$$

where  $\alpha_{xx}, \alpha_{yy} > 0$  and  $\alpha_{xx}\alpha_{yy} - \alpha_{xy}^2 > 0$  thus ensuring that  $\mathcal{L}$  is elliptic and invertible. The vector  $\boldsymbol{\xi} = [\tau, \boldsymbol{\alpha}, \boldsymbol{\gamma}] \in \mathbb{R}^7$  collect all the trainable parameters. The input field  $a$  is mapped to the

embedding  $\tilde{v}$  by means of the operator  $\mathcal{R} : \mathcal{A} \rightarrow \mathbb{R}^{d_v}$  consisting of a convolution operation Eq. (11) with  $1 \times 1$  filters. In this way, the initial condition of Eq. (12) is obtained and the parabolic PDE is solved. Finally, the output of the convolution is obtained by taking the derivative of  $\tilde{v}(\tau, \mathbf{x})$  in the direction  $\gamma$ . So, introducing a suitable uniform discretization of the domain  $\Omega$ , solving Eq. (12) by means of Fast Fourier Transform (FFT) and differentiating the solution in the direction  $\gamma$  actually consists of applying the mesh-free convolution [Zakariaei et al., 2025].

We validate the proposed algorithm by employing mesh-free convolutional neural networks on the test cases Eqs. (7) and (8). In particular, to take into account advection and incorporate the knowledge we have about the system in Eq. (8), we add to the mesh-free convolutional kernel a term of the form [Ruthotto and Haber, 2020]:

$$\psi_x[-1, 0, 1] \quad \text{and} \quad \psi_y[1, 0, -1],$$

that is we add a second convolutional layers by fixing their weights equal to the second order finite difference discretization of the advection term and we multiply the output by a trainable parameter in each direction of the domain. Then, the vector of all trainable parameters becomes  $\xi = [\tau, \alpha, \gamma, \psi] \in \mathbb{R}^9$  for each mesh-free convolutional layer.

Table 4: *Darcy problem*. Baselines training time per epoch and test loss by varying the resolution  $R$ .

Resolution	$R = 15$	$R = 30$	$R = 60$	$R = 120$	$R = 241$
Train epoch time [s]	0.81	0.83	0.91	1.26	3.96
Test loss [ $\times 10^{-2}$ ]	15.2	2.5	2.0	2.0	1.8

To obtain the baselines, we first run standard SGD to approximate the solution operator on the resolutions  $\{R_m\}_{m=1}^5 = \{241, 120, 60, 30, 15\}$  and the results are the ones reported in Table 4. The training time per epoch and the testing loss values obtained by means of our proposed training paradigm, with  $m = 3$  levels and hierarchy as pairing strategy, are gathered in Table 5. As expected, by increasing the multiplier  $\delta$  the test loss increases as the epoch train time decreases because a smaller amount of fine training data is used. We also report the test related to the use of the optimal number of samples per resolution  $N_i^*$ , see, e.g., [Giles, 2015] (in our case  $k = 1$  and  $\gamma = 1$ ). Moreover, we select  $\delta = \delta^* = 2$ . This configuration is the one providing the best performance, in terms of accuracy with respect to the baseline with  $R = 241$ , and it is related to the fact that even if  $N_i^* \approx 8N_{i-1}^*$  we are employing  $\delta = 2$  instead of  $\delta = 8$ ; indeed, in the latter case, during one epoch less batches of fine resolution data are seen with respect to the number of batches of coarse data. As the value for  $\delta$  increases the gap between the number of batches of fine and coarse data increases making the gradients' estimates more and more biased towards large-scales, or in the same way, the exposure to fine-scale corrections is limited.

Table 5: *Darcy problem*. MLMC training time per epoch and test loss by varying  $\delta$  and  $m = 3$ .

Parameter $\delta$	$\delta = 8$	$\delta = 4$	$\delta = 2$	$\delta = 1.5$	$\delta = 1$	$\delta^* = 2$
Train epoch time [s]	<b>0.19</b>	<b>0.55</b>	1.25	1.66	2.48	<b>0.60</b>
Test loss [ $\times 10^{-2}$ ]	<b>7.8</b>	<b>4.7</b>	3.3	3.2	3.1	<b>2.5</b>

In Fig. 7, we report the comparison among the ground truth data and the approximation obtained by means of traditional SGD, both with  $R = 241$ , and the MLMC approximated solution, with hierarchy pairing strategy,  $m^* = 3$  and  $\delta^* = 2$ , for different testing instances of the diffusion coefficients.

To obtain the baseline quantities for the advection-diffusion test-case Eq. (8), we just consider resolution  $R = 300$ , since smaller ones did not provide an acceptable accuracy, considering the current model and expressivity. So, in this case, the goal is to show that coarser data, which it is not possible to use per se, can be actually exploited in the MLMC paradigm to capture large-scale effects together with finer correction terms. The baseline epoch training time is  $8.97s$  while the testing loss is equal to 0.08%. In Fig. 7, we compare the ground truth data (second row), the baseline SGD approximation (third row), and the approximated solution obtained by means of MLMC with  $m = 3$  and  $\delta = 2$ , resulting in a test loss of 2.1% and a computational speed-up equal to 4, for different instances of the source term.

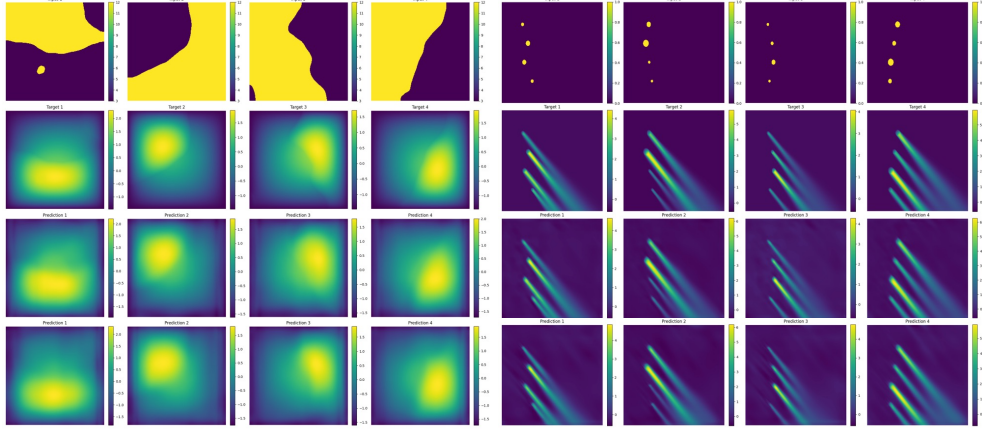


Figure 7: *Darcy (left) and advection-diffusion (right) problems.* Comparison between the ground truth data (second row), the SGD solution (third row) and the MLMC approximation (fourth row) for different source inputs (first row).

## C.2 Fourier neural operator

We compare the ground truth data with the FNO approximation obtained through the MLMC training algorithm in Fig. 8 by considering the values of  $m, \delta$  giving the best performance in terms of accuracy and computational time, respectively. More precisely, the third row refers to the choice  $m = 4$  and  $\delta = 1$ , using the random pairing strategy, while the fourth one to  $m = 4$  and  $\delta = 8$ , always using random as pairing strategy. Regarding the latter, the error with respect to the ground truth data is about 3.56% and the epoch training time is 0.054s, leading to a speed-up almost equal to 74 with respect to the baseline data with  $R = 241$  and 8 with respect to the baseline with  $R = 30$ .

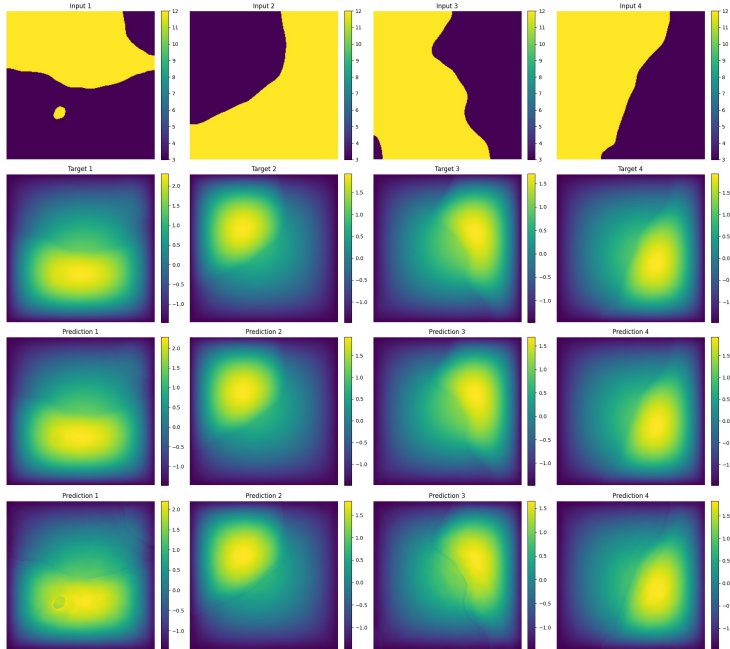


Figure 8: *Darcy test problems.* Comparison between the ground truth data (second row), and the MLMC solutions with  $m = 4$  and  $\delta = 1$  (third row), and  $m = 4$  and  $\delta = 8$  (fourth row).